

# Arithmetic with X-ray images of galaxy clusters: effective equation of state for small-scale perturbations in the ICM

E. Churazov,<sup>1,2</sup> P. Arevalo<sup>3</sup>, W. Forman<sup>4</sup>, C. Jones<sup>4</sup>, A. Schekochihin<sup>5,6</sup>,  
A. Vikhlinin,<sup>4</sup> I. Zhuravleva<sup>7,8</sup>

<sup>1</sup> *Max-Planck-Institut für Astrophysik (MPA), Karl-Schwarzschild-Strasse 1, 85741 Garching, Germany*

<sup>2</sup> *Space Research Institute (IKI), Profsoyuznaya 84/32, Moscow 117997, Russia*

<sup>3</sup> *Instituto de Física y Astronomía, Facultad de Ciencias, Universidad de Valparaíso, Gran Bretaña N 1111, Playa Ancha, Valparaíso, Chile*

<sup>4</sup> *Harvard-Smithsonian Center for Astrophysics, 60 Garden St., Cambridge, MA 02138, USA*

<sup>5</sup> *Rudolf Peierls Centre for Theoretical Physics, University of Oxford, 1 Keble Rd, Oxford OX1 3NP, UK*

<sup>6</sup> *Merton College, University of Oxford, Merton St, Oxford OX1 4JD, UK*

<sup>7</sup> *Kavli Institute for Particle Astrophysics and Cosmology, Stanford University, 452 Lomita Mall, Stanford, California 94305-4085, USA*

<sup>8</sup> *Department of Physics, Stanford University, 382 Via Pueblo Mall, Stanford, California 94305-4060, USA*

31 May 2016

## ABSTRACT

We discuss a novel technique of manipulating X-ray images of galaxy clusters to reveal the nature of small-scale density/temperature perturbations in the intra cluster medium (ICM). As we show, this technique can be used to differentiate between sound waves and isobaric perturbations in Chandra images of the Perseus and M87/Virgo clusters. The comparison of the manipulated images with the radio data and with the results of detailed spectral analysis shows that this approach successfully classifies the types of perturbations and helps to reveal their nature. For the central regions (5-100 kpc) of the M87 and Perseus clusters this analysis suggests that observed images are dominated by isobaric perturbations, followed by perturbations caused by bubbles of relativistic plasma and weak shocks. Such a hierarchy is best explained in a “slow” AGN feedback scenario, when much of the mechanical energy output of a central black hole is captured by the bubble enthalpy that is gradually released during buoyant rise of the bubbles. The “image arithmetic” works best for prominent structure and for datasets with excellent statistics, visualizing the perturbations with a given effective equation of state. The same approach can be extended to faint perturbations via cross-spectrum analysis of surface brightness fluctuations in X-ray images in different energy bands.

## Key words:

## 1 INTRODUCTION

Apart from global density and temperature radial profiles, fundamental information on the physics of the ICM is contained in the small-scale deviations of the ICM properties from this global model. Understanding the nature of the perturbations is particularly important to constrain conduction and viscosity in hot gaseous atmospheres of galaxies, groups, and clusters and to probe physical mechanisms driving these perturbations.

Density and temperature perturbations of the ICM are found in simulations (e.g., Kawahara et al. 2007; Zhuravl-

eva et al. 2013; Roncarelli et al. 2013) and observations (e.g., Markevitch 1996). They reflect the non-stationary nature of a cluster and can be caused by a variety of processes, ranging from mergers to radiative cooling of the cluster gas. Especially rich substructure is found in the cores of relaxed clusters, where AGN feedback plays a key role (e.g., Boehringer et al. 1993; Churazov et al. 2000; Fabian et al. 2000; McNamara et al. 2000; Jones et al. 2002; Forman et al. 2007). The key question is an objective characterization of these perturbations. Properties of the perturbations not only reflect the driving mechanisms behind them, but also depend on

the microphysics of the ICM, in particular, on the thermal conduction and viscosity (e.g., Roediger et al. 2013; Gaspari & Churazov 2013; ZuHone et al. 2015).

One possible way of revealing the nature of the perturbations is via measuring the correlation between density and temperature fluctuations, to construct an effective “equation of state” for the perturbations. For example, a positive correlation between temperature and density fluctuations suggests that the gas is adiabatically compressed (e.g., Schuecker et al. 2004), while a negative correlation hints at isobaric perturbations, associated with entropy fluctuations (e.g., Markevitch, Sarazin, & Irwin 1996; Churazov et al. 2003; Forman et al. 2007). Various flavours of such analysis have been done (e.g., Shibata et al. 2001; Schuecker et al. 2004; Finoguenov, Böhringer, & Zhang 2005; Kawahara et al. 2008; Gu et al. 2009; Arévalo et al. 2016; Zhuravleva et al. 2016; Hofmann et al. 2016). Here we discuss a novel technique of manipulating X-ray images of galaxy clusters to reveal the nature of small-scale density/temperature perturbations in the ICM.

The structure of the paper is as follows. In §2 we discuss a modification of the hardness-ratio technique. We factorize the hardness ratio map into large-scale and small-scale maps, using Chandra data on the Perseus cluster for illustration. In the rest of the paper we use (and further modify) the small-scale component of the hardness ratio. In §3 we predict the response in different energy bands to linear perturbations of the ICM thermodynamic properties. In §4 we suggest a way to manipulate X-ray images in order to suppress a particular type of perturbations and provide illustrative examples in §5. The results are summarized in §6.

## 2 PROJECTED HARDNESS-RATIO AND TEMPERATURE MAPS

Generating projected temperature maps can be straightforwardly done by partitioning the image into regions with a sufficient number of photon counts, extracting spectra and then approximating them with a model of optically thin plasma. This procedure can be much simplified if the temperature variations are not very large. We describe below two techniques that provide a quick replacement for an often lengthy direct fitting procedures.

### 2.1 Taylor expansion of the temperature dependence

One possible way of quickly constructing a projected temperature map of a cluster (Churazov et al. 1996) is to make a Taylor expansion of the plasma emissivity  $\epsilon(E, T)$  with respect to small changes of temperature  $T$ :

$$\epsilon(E, T) \approx \epsilon(E, T_0) + \left. \frac{\partial \epsilon(E, T)}{\partial T} \right|_{T_0} \delta T, \quad (1)$$

where  $E$  is the photon energy,  $\delta T = T - T_0$  is a small deviation of temperature from a reference value. The functions of energy in the r.h.s.,  $\epsilon(E, T_0)$  and  $\left. \frac{\partial \epsilon(E, T)}{\partial T} \right|_{T_0}$ , can be easily generated using the Astrophysical Plasma Emission

Code (APEC) (Smith et al. 2001) or the SPEX package (Kaastra, Mewe, & Nieuwenhuijzen 1996). In practice, it is convenient to replace  $\frac{\partial \epsilon(E, T)}{\partial T}$  with a “macroscopic derivative”  $\frac{\epsilon(E, T_2) - \epsilon(E, T_1)}{T_2 - T_1}$ , where  $T_1$  and  $T_2$  are the values of temperature bracketing the expected range of temperature variations in a given cluster. Then eq. (1) can be re-written as

$$\epsilon(E, T) \approx a_1 \epsilon(E, T_1) + a_2 \epsilon(E, T_2), \quad (2)$$

where  $\epsilon(E, T_1)$  and  $\epsilon(E, T_2)$  are given and  $a_1$  and  $a_2$  are the two free parameters of the model. Fitting the observed spectrum to eq. 2 reduces to a trivial linear problem that is computationally fast (based on the calculation of the scalar product of observed counts with reference models  $\epsilon(E, T_1)$  and  $\epsilon(E, T_2)$ ) and can be done in the highest resolution pixels, even if there are only a few counts in these pixels. Once the maps of  $a_1$  and  $a_2$  are generated, they can be (adaptively) smoothed and combined to determine the value of the temperature, which in the simplest form is

$$T = \frac{a_1 T_1 + a_2 T_2}{a_1 + a_2}, \quad (3)$$

see Churazov et al. (1996) for a more accurate version of this expression, that ensures that the value of  $T$  is recovered exactly not only at the boundaries of the  $[T_1 : T_2]$  interval, but also at  $T = (T_1 + T_2)/2$ . A comparison with the results of direct fitting has shown that despite the simplicity of the method, the derived values of temperature are accurate and have similar statistical uncertainty. The temperature map of the Perseus cluster obtained from Chandra observations, in this way, is shown in the left panel of Fig. 1.

As a caveat, we mention that this procedure assumes that all other parameters, e.g., abundance of heavy elements or low energy photoelectric absorption, do not affect the hardness ratio. In fact, in the very core of the Perseus cluster there are clear signs of strong low-energy absorption features (see, e.g., Fabian et al. 2000) that do affect hardness ratio (see text and figures below). In the rest of the paper we ignore the regions that are known to be affected by the low energy absorption.

### 2.2 Modified hardness ratio

An even simpler approach is to use hardness-ratio maps, based on the images in two sufficiently different energy bands, which we designate below as  $s$  and  $h$ , corresponding to energy intervals  $[E_{s,1} : E_{s,2}]$   $[E_{h,1} : E_{h,2}]$ . Once again, the assumption that the perturbations are small allows one to rewrite the expression for the hardness ratio  $H$  as

$$H(x, y) = \frac{I_h(x, y)}{I_s(x, y)} = \frac{I_h^0(x, y) \left(1 + \frac{\delta I_h(x, y)}{I_h^0(x, y)}\right)}{I_s^0(x, y) \left(1 + \frac{\delta I_s(x, y)}{I_s^0(x, y)}\right)} \approx \frac{I_h^0(x, y)}{I_s^0(x, y)} \left(1 + \frac{\delta I_h(x, y)}{I_h^0(x, y)} - \frac{\delta I_s(x, y)}{I_s^0(x, y)}\right), \quad (4)$$

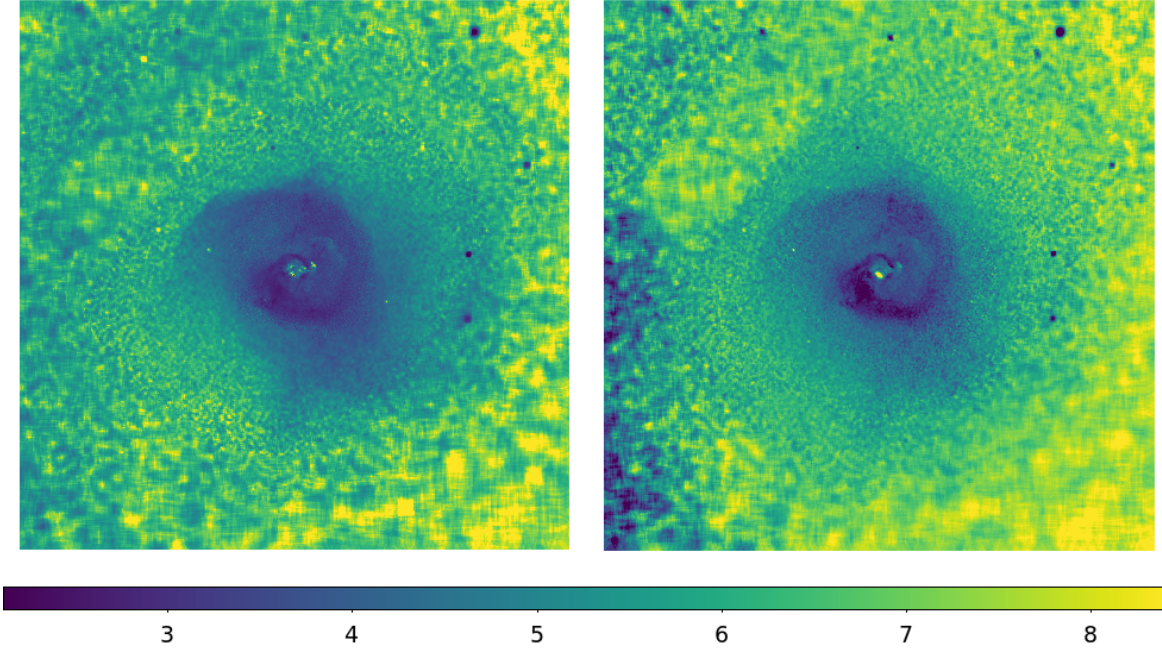


**Figure 1.** Projected temperature and hardness ratio maps ( $16' \times 16'$ ) of the Perseus cluster. **Left:** The temperature map calculated from Chandra data using the approach described in Churazov et al. (1996). Small dark spots, e.g., in the upper-right corner, correspond to background AGNs that were not excised when constructing the temperature map. Bright yellow patches near the center are due to low-energy absorption features in the Perseus core (Fabian et al. 2000). **Right:** Hardness-ratio map based on eq. (4) using the two energy bands 0.5-3.5 keV and 3.5-7.5 keV.

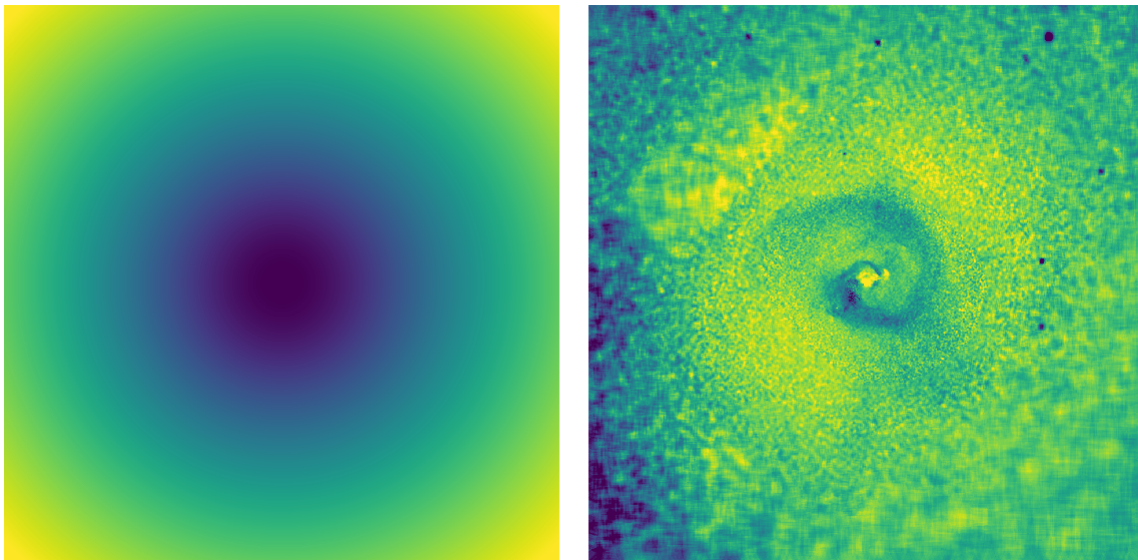


**Figure 2.** Decomposition of hardness ratio  $H$  into large-scale  $H_g$  and small-scale  $H_p$  components,  $H = H_g H_p$  [see, eq. (4) and §2.2]. **Left:** Large scale radial dependence of the hardness ratio  $H_g$ , calculated as the ratio of best-fitting beta models for the 0.5-3.5 and 3.5-7.5 keV bands  $H_g = \frac{I_h^0(x, y)}{I_s^0(x, y)}$ . **Right:** Small-scale variations of the hardness ratio  $H_p = \left( 1 + \frac{\delta I_h(x, y)}{I_h^0(x, y)} - \frac{\delta I_s(x, y)}{I_s^0(x, y)} \right)$ . The value of  $H_p$  characterizes temperature variations, associated with departures from symmetric smooth models. The image has been adaptively smoothed with a boxcar filter. A bright feature close to the nucleus in the right panel is caused by cold gas absorption (see, e.g., Fabian et al. 2000). A boxy structure in the top-left corner corresponds to the underexposed area compared to the central region, which is covered with multiple long pointings.

where  $I_h$  and  $I_s$  are the projected X-ray images in the hard and soft band respectively:

$$I_{s,h}(x, y) = \int n^2 \Lambda_{s,h}(T) dz, \quad (5)$$

$$\Lambda_{s,h}(T) = \int_{s,h} \epsilon(E, T) dE, \quad (6)$$

where  $n = n(x, y, z)$  is the gas density; the integration in eq. (5) is over the line of sight (along the  $z$  axis), while in eq. (6) the integration is over the energy intervals, corresponding to the  $s$  or  $h$  bands respectively.  $I_h^0$  and  $I_s^0$  are suitable simple models, describing global radial profiles, and  $\delta I_h = I_h - I_h^0$  and  $\delta I_s = I_s - I_s^0$  are the deviations of X-ray images from these simple models. For instance, a  $\beta$ -model (Cavaliere & Fusco-Femiano 1978)

$$I^0(x, y) = C \left[ 1 + \left( \frac{\sqrt{x^2 + y^2}}{r_c} \right)^2 \right]^{-3\beta+1/2} \quad (7)$$

can be used as  $I_h^0$  and  $I_s^0$ . For a cluster with a radial temperature gradient, not only the normalization  $C$ , but also other parameters,  $\beta$  and  $r_c$ , of the  $\beta$ -models describing  $I_h^0$  and  $I_s^0$  may be different.

One can see from eq. (4) that if  $\frac{\delta I_h(x, y)}{I_h^0(x, y)} \ll 1$  and  $\frac{\delta I_s(x, y)}{I_s^0(x, y)} \ll 1$ , then the calculation of the hardness ratio can be factorized into two terms  $H = H_g H_p$  [see Fig. 2], where the first term  $H_g = \frac{I_h^0(x, y)}{I_s^0(x, y)}$  describes a global profile and the second term  $H_p$  [the term in parentheses in eq. (4)] describes the variations of the hardness ratio associated with deviations of observed images from the global  $I_h^0$  and  $I_s^0$  models. This  $H_p$  term can be evaluated as the difference between (adaptively) smoothed images  $\frac{\delta I_h(x, y)}{I_h^0(x, y)}$  and  $\frac{\delta I_s(x, y)}{I_s^0(x, y)}$ . The resulting hardness ratio  $H = H_g H_p$  is shown in the right panel of Fig. 1. Of course, if one is interested in the temperature map, these values of  $H$  have to be converted<sup>1</sup> to  $T$ , unlike in the procedure described in the previous section, where the temperature is obtained directly.

Notice that  $H_p$  involves only a division of the data by a smooth global model. This means that a notorious problem of having noisy data in the denominator is avoided by a suitable choice of global models  $I_h^0$  and  $I_s^0$ , subject to the condition that deviations from these models are small. The implication is that we can avoid excessive smoothing of observed images needed to suppress noise in the expression  $H = I_h/I_s$ .

### 3 ICM EMISSIVITY AND PROJECTED X-RAY IMAGES

In the above section we have factorized the hardness ratio  $H = H_g H_p$  into “global” and “perturbed” parts. Below we

use a similar approach to single out and characterize the properties of the ICM perturbations on small scales.

As a first step, we want to calculate the variations of the plasma volume emissivity in a given band  $f = n^2 \Lambda_B(T)$ , due to the density and temperature variations. Here the index  $B$  corresponds to one of the bands ( $s$  or  $h$ ). For the purposes of this paper, we assume that the gas density  $n$  and temperature  $T$  distributions in a cluster can be factorized into an “unperturbed” spherically symmetric model ( $n_0(r)$  and  $T_0(r)$ ) and small-amplitude perturbations with respect to this model:

$$n(x, y, z) = n_0(r) \times [1 + \delta_n(x, y, z)] \quad (8)$$

$$T(x, y, z) = T_0(r) \times [1 + \delta_T(x, y, z)],$$

where  $r = \sqrt{x^2 + y^2 + z^2}$ . We further assume that the relative perturbations  $\delta_n$  and  $\delta_T$  are not independent, but associated with a particular type of density/temperature perturbation characterized by the correlated changes of both quantities

$$\frac{d \ln T}{d \ln n} \equiv \alpha, \quad (9)$$

so the relation between small perturbations  $\delta_n$  and  $\delta_T$  has the form  $\delta_T = \alpha \delta_n$ . Below we interpret perturbations with different  $\alpha$  as perturbations having different effective equations of state (EoS). Note, that this is not necessarily the EoS in the thermodynamic sense. By virtue of eq. (8) we probe deviations of the gas properties from a smooth global model at a given position in a cluster. Thus, the effective EoS characterizes the fluctuations of gas properties for gas lumps located at the same radial distance from the center (at least for spherically symmetric models), rather than the changes of the thermodynamic properties of the same gas lump.

In this language,  $\alpha = \gamma - 1$ , where  $\gamma$  is the effective adiabatic index of a perturbation when the pressure-density relation is  $P \propto \rho^\gamma$ . For the purpose of this paper, we restrict the set of perturbation types to adiabatic, isobaric and isothermal:

$$\begin{aligned} \alpha &= 2/3 && \text{adiabatic, } \gamma = 5/3 \\ \alpha &= -1 && \text{isobaric, } \gamma = 0 \\ \alpha &= 0 && \text{isothermal, } \gamma = 1. \end{aligned} \quad (10)$$

For example, adiabatic perturbations can be caused by sound waves (weak shocks) going through the gas. Isobaric perturbations, associated with entropy variations of the gas lumps in pressure equilibrium with each other, could be due to slow displacement of fluid elements from their equilibrium positions (e.g., gravity waves). Apparently “isothermal” perturbations could be due to bubbles of relativistic plasma, which are devoid of X-ray emitting gas; if the pressure of the relativistic plasma matches the ambient gas pressure, the bubbles will be seen as X-ray-dim “cavities”, suggesting a drop of thermal-gas density without apparent changes in the gas temperature.

As in §2 we use the APEC model (Smith et al. 2001) as implemented in XSPEC (Arnaud 1996) to derive the energy dependent plasma emissivity  $\epsilon(E, T)$ , fixing the abundance of heavy elements to 0.4 solar. Unlike eq. (6), we now spe-

<sup>1</sup> This conversion is straightforward, since the expected hardness ratio as a function of temperature can be easily predicted.

cialize the emissivity  $\Lambda_B(T)$  in a given energy band  $B$  to the *CHANDRA* ACIS-I instrument. Namely, we convolve  $\epsilon(E, T)$  with the ACIS-I response (including effective area) and then integrate over energy channels. Examples of the temperature-dependent emissivity  $\Lambda_B(T)$  for several representative energy bands are shown in Fig. 3.

We can now predict the relative perturbation  $\delta_f$  of the plasma volume emissivity (X-ray flux per  $\text{cm}^3$ )  $f = n^2 \Lambda_B(T) = f_0(1 + \delta f)$  in a given *CHANDRA* band  $B$  for a particular type of perturbation, characterized by the parameter  $\alpha$  [see eq. (9)]

$$\begin{aligned} \delta_f &\approx \left[ 2 + \frac{d \ln T}{d \ln n} \frac{d \ln \Lambda_B}{d \ln T} \Big|_{T_0} \right] \delta_n \\ &\approx \left[ 2 + \alpha \frac{d \ln \Lambda_B}{d \ln T} \Big|_{T_0} \right] \delta_n. \end{aligned} \quad (11)$$

Since the value  $\frac{d \ln \Lambda_B}{d \ln T}$  is known for each energy band (see Figs. 3 and 4), for a given  $\delta n$  the amplitude of the flux perturbations can be predicted for each type of perturbation, i.e. for different  $\alpha$ . If the amplitude is measured in two energy bands  $B_1$  and  $B_2$  (having different  $\frac{d \ln \Lambda_B}{d \ln T}$ ) one can construct a linear combination of the amplitudes that emphasizes (or suppresses) a particular type of perturbation. The coefficients for such linear combinations can be derived from the expected ratio  $R_f$  of fluxes in these two bands

$$R_f = \frac{\delta_{f_2}}{\delta_{f_1}} = \frac{\left[ 2 + \alpha \left( \frac{d \ln \Lambda_{B_2}}{d \ln T} \right) \Big|_{T_0} \right]}{\left[ 2 + \alpha \left( \frac{d \ln \Lambda_{B_1}}{d \ln T} \right) \Big|_{T_0} \right]}. \quad (12)$$

A particular example of expected ratios for different types of perturbations is shown in Fig. 5 for  $B_1 = 0.5\text{-}3.5$  keV and  $B_2 = 3.5\text{-}7.5$  keV.

Of course, observations provide us projected images in different energy bands, rather than direct measurements of volume emissivity/flux variations as in eq. (11). Handling projected images is discussed in the next section.

### 3.1 Projected X-ray images

An observed X-ray image in a given energy band  $B$  is the projection of the volume emissivity along the line of sight

$$\begin{aligned} I_B(x, y) &= \int f dz \\ &= \int n_0^2 \Lambda_B(T_0) \left( 1 + \left[ 2 + \alpha \left( \frac{d \ln \Lambda_B}{d \ln T} \right) \right] \delta_n \right) dz. \end{aligned} \quad (13)$$

For an unperturbed gas distribution, i.e., when  $\delta_n = 0$ , the above expression provides a smooth model image in each band

$$I_B^0(x, y) = \int n_0^2 \Lambda_B(T_0) dz. \quad (14)$$

The ratio  $J_B(x, y)$  of the observed image to the model image provides the measure of surface brightness fluctuations relative to the model in a given band

$$J_B(x, y) = \frac{I_B(x, y)}{I_B^0(x, y)} - 1. \quad (15)$$

Let us consider a small perturbation that is located at  $z = z_0$  along the line of sight, and has a small spatial extent  $\Delta z$ . Then

$$J_B(x, y) = \frac{n_0^2(r) \Lambda_B(T_0(r)) \delta_n \Delta z \left[ 2 + \alpha \left( \frac{d \ln \Lambda_B}{d \ln T} \right) \Big|_{T_0(r)} \right]}{I_B^0(x, y)}, \quad (16)$$

where  $r = \sqrt{x^2 + y^2 + z_0^2}$ . We now consider several limiting cases.

If the cluster is globally isothermal, then  $T_0(r) = \text{const}$ ,  $\Lambda_B(r) = \text{const}$  and  $\left[ 2 + \alpha \left( \frac{d \ln \Lambda_B}{d \ln T} \right) \Big|_{T_0(r)} \right] = \text{const}$ . With this assumption the ratio of amplitudes  $J$  in two bands ( $B_1$  and  $B_2$ ) at any point of the image is simply

$$R(x, y) = R_f, \quad (17)$$

where  $R_f$  is give by eq. (12), see also Fig. 5. Notice that  $R(x, y)$  does not depend on the position or the amplitude of the perturbation and is therefore a direct proxy for  $\alpha$  – the type of the perturbation.

If the cluster is not isothermal, as is the case for typical cool-core clusters, then the ratio  $\frac{J_{B_2}}{J_{B_1}}$  will be position dependent. It is therefore useful to introduce an additional position-dependent correction  $\zeta_B(x, y)$  to eq. (16) to at least partly mitigate the problem

$$\tilde{J}_B(x, y) = J_B(x, y) \zeta_B(x, y), \quad (18)$$

so that in the ratio  $\frac{\tilde{J}_{B_2}}{\tilde{J}_{B_1}}$  the position-dependence approximately cancels out.

The simplest correction comes from the assumption that the observed perturbation is located close to the mid-plane of the cluster, i.e., at  $z_0 = 0$ . In this approximation,

$$\zeta_B(x, y) \propto \frac{I_B^0(x, y)}{\Lambda_B(T_0(r))}. \quad (19)$$

From eq. (16) it is clear that such corrections would recover the desired property of the ratio  $R(x, y) = \frac{\tilde{J}_{B_2}}{\tilde{J}_{B_1}}$  to be sensitive only to the value of  $\alpha$ . Since the perturbations located close to the mid-plane are favoured by the  $n^2$  dependence of the gas volume emissivity, this correction factor is expected to work well. One can then use  $R(x, y)$  as a tool to classify individual perturbations according to their effective EoS.

Alternatively, one can assume that perturbations are small and volume-filling (i.e., that they are quasi-uniformly distributed over the cluster volume) and calculate an averaged correction, weighted with the  $n_0^2$  term to account for the suppression of their contributions to the image due to projection effects (see, e.g., Churazov et al. 2012). Of course, in this case the correction factor works only ‘‘on average’’. In practice, for realistic temperature profiles, the two forms of the correction factor are not very different, because  $n_0^2$  term favours perturbations located close to mid-plane.

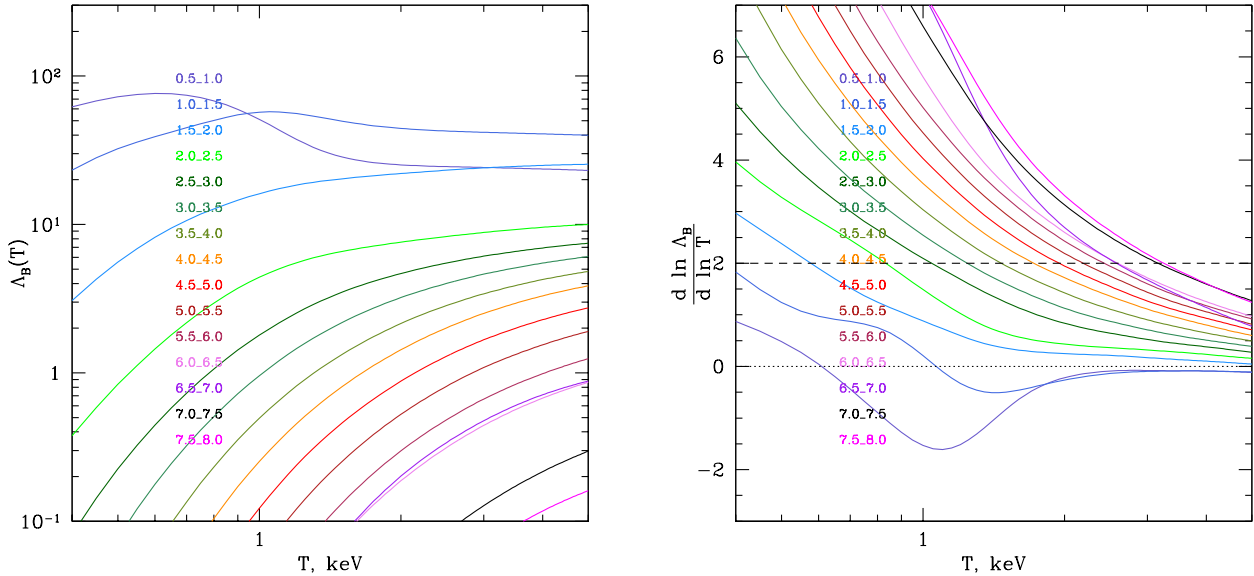


**Figure 3.** **Left:** X-ray emissivity as a function of temperature. The emissivity (in arbitrary units) is calculated in half keV wide bands of ACIS-I (energy increases from top to bottom and is shown in the legend), using the APEC model of optically thin plasma with the abundance of heavy elements taken to be 0.4 solar. **Right:** Logarithmic derivative of the emissivity over temperature  $\frac{d \ln \epsilon_B}{d \ln T}$  for the same set of bands as in the left panel. Energy increases from bottom to top. As expected, at temperatures  $\gtrsim 2$  keV the emissivity in the soft band (below  $\lesssim 2.5$  keV) does not depend on temperature. For harder bands, this is not true. The dashed horizontal line shows for each band at what temperature  $\frac{d \ln \epsilon_B}{d \ln T} \approx 2$ . If this condition is satisfied, then pure isobaric perturbations will not be visible in this band (Forman et al. 2007, ; see Figs, 10 and 11). Note also that for low cluster temperatures ( $T \lesssim 1.5$  keV), the derivative is negative in the softest (0.5-1.0 keV) band. This effectively decreases the sensitivity of images in this band to adiabatic to adiabatic perturbations (see eq. [14]).

## 4 ARITHMETIC WITH X-RAY IMAGES

### 4.1 Energy bands “free” from isobaric perturbations

From eq. (11), it is clear that, if, for a given  $T$ , the value of  $\frac{d \ln \Lambda_B}{d \ln T}$  is close to 2, then for isobaric perturbations (i.e.,  $\alpha = -1$ ) no flux variations are expected. The dashed horizontal lines in the right panel of Fig. 3 and in Fig. 4 correspond to  $\left(\frac{d \ln \Lambda_B}{d \ln T}\right) = 2$ . For instance, for the gas temperature  $T \sim 2$  keV the isobaric perturbations should not be present in the images in the 3.5-7.5 keV band (see Fig. 4). This approach was used by Forman et al. (2007) for M87 ( $T_0 \sim 2$  keV) to avoid contamination of images by prominent isobaric structures and to reveal quasi-spherical weak shocks around the nucleus. In principle, for any given gas temperature one can try to select an appropriate band, but

the limited energy band accessible to Chandra makes it difficult to handle hot clusters.

While it is possible to generate images free of isobaric perturbations, for isothermal and adiabatic processes this procedure will not work<sup>2</sup>. A more promising approach is to combine two images in different energy bands, as is discussed below.

### 4.2 Arithmetic with two images

We now combine two flattened images  $J_{B_1}$  and  $J_{B_2}$  (or corrected images  $\tilde{J}_{B_1}$  and  $\tilde{J}_{B_2}$ ) in such a way that perturbations with a given effective EoS of state (i.e., given  $\alpha$ ) are

<sup>2</sup> Note, however, that for  $T \sim 1$  keV, the contribution of adiabatic processes is expected to be severely attenuated in the very soft energy band, where  $\frac{d \ln \Lambda_B}{d \ln T}$  is negative (see Fig. 3).

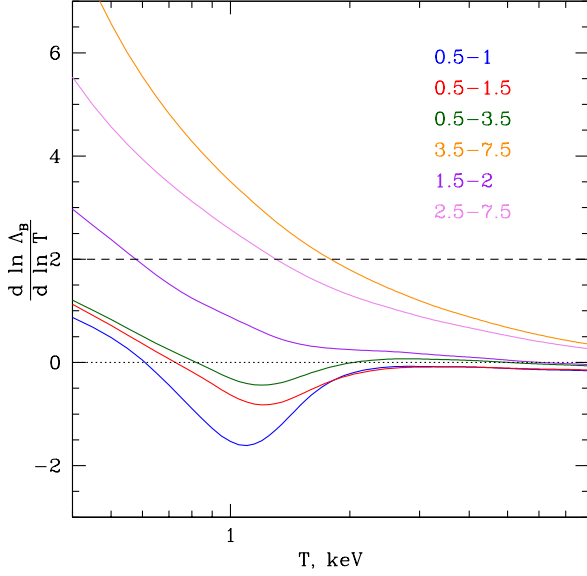


**Figure 4.** The same as in the Fig. 3, but for broader energy bands.

cancelled in the combined image

$$X = c_{B_1} J_{B_1} + c_{B_2} J_{B_2}, \quad (20)$$

where coefficients  $c_{B_1}$  and  $c_{B_2}$  satisfy the condition

$$c_{B_1} \left[ 2 + \alpha_0 \left( \frac{d \ln \Lambda_{B_1}}{d \ln T} \right) \right] + c_{B_2} \left[ 2 + \alpha_0 \left( \frac{d \ln \Lambda_{B_2}}{d \ln T} \right) \right] = 0, \quad (21)$$

where  $\alpha_0$  characterizes perturbations that we wish to remove. It is useful to impose an additional constraint on  $c_{B_1}$  and  $c_{B_2}$

$$c_{B_1} \left[ 2 + \alpha_R \left( \frac{d \ln \Lambda_{B_1}}{d \ln T} \right) \right] + c_{B_2} \left[ 2 + \alpha_R \left( \frac{d \ln \Lambda_{B_2}}{d \ln T} \right) \right] = 1, \quad (22)$$

where  $\alpha_R \neq \alpha_0$  can be chosen arbitrarily. Then the amplitudes of perturbations having effective an EoS characterized by  $\alpha_R$  will reflect pure density variations associated with this particular type of perturbation. As is well-known (see §3 and Fig. 3), in the soft band (e.g., 0.5-2 keV) the observed perturbations are largely sensitive to density perturbations, since the emissivity in this band weakly depends on temperature. From eqs. 16, 20, 21, 22, specializing for simplicity to the case of an isothermal cluster, i.e.,  $\frac{n_0^2(r) \Lambda_{B_1}(T_0(r))}{I_{B_1}^0(x, y)} = \frac{n_0^2(r) \Lambda_{B_2}(T_0(r))}{I_{B_2}^0(x, y)}$ , the resulting amplitude of perturbations, characterized by a given  $\alpha$  is

$$X = \frac{n_0^2(r) \Lambda_B(T_0(r))}{I_B^0(x, y)} A_\alpha \delta_n \Delta z, \quad (23)$$

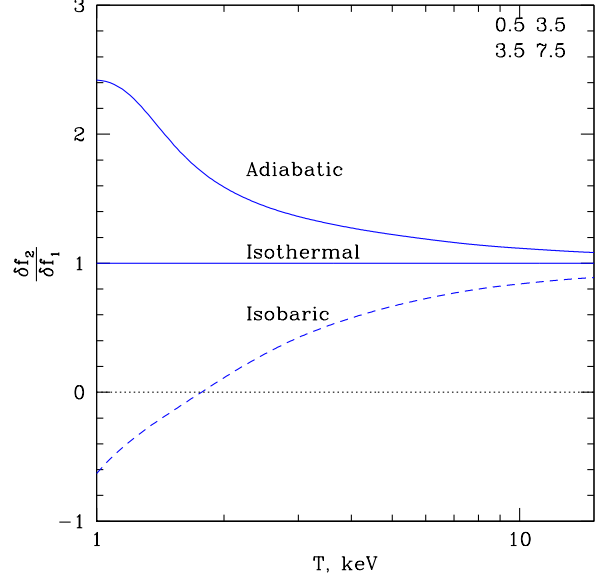


**Figure 5.** Ratio of fluxes (volume emissivities) for different types of perturbations as a function of temperature for the 0.5-3.5 and 3.5-7.5 keV bands. The top curve is for adiabatic perturbations, predicting that the amplitude is larger in the hard band. The bottom curve is for isobaric perturbations, in which case the amplitude in the hard band is lower than in the soft band. In particular, the amplitude is close to zero in the 3.5-7.5 keV gas at  $T \sim 2$  keV. At lower temperatures, the hard-band amplitude even becomes negative, i.e., increasing density causes the 3.5-7.5 keV flux to drop. The solid horizontal line corresponds to isothermal perturbations, which produce the same amplitude in both bands.

where

$$A_\alpha = \frac{\alpha - \alpha_0}{\alpha_R - \alpha_0}. \quad (24)$$

Comparison with eq. (16) shows that in the manipulated image  $X$ , the perturbations having  $\alpha = \alpha_0$  are suppressed ( $A_\alpha = 0$ ), while the perturbations with  $\alpha = \alpha_R$  have  $A_\alpha = 1$ , i.e., their amplitude reflects pure density variations<sup>3</sup>. The values of the factor  $A_\alpha$  in eq. (23) for perturbations characterized by  $\alpha$  (given  $\alpha_R$  and  $\alpha_0$ ) are calculated in Table 1, using our standard set of values  $\alpha = \{2/3, 0, -1\}$ .

Note that the above procedure can eliminate from our images the perturbations with any given EoS even if several perturbations with different EoS's are projected on top

<sup>3</sup> Note, that in eq. (16) the amplitude of flux caused by a pure density perturbation will be factor of 2 higher than in eq. (23). This is because we set the r.h.s. of eq. (22) to 1, rather than 2.

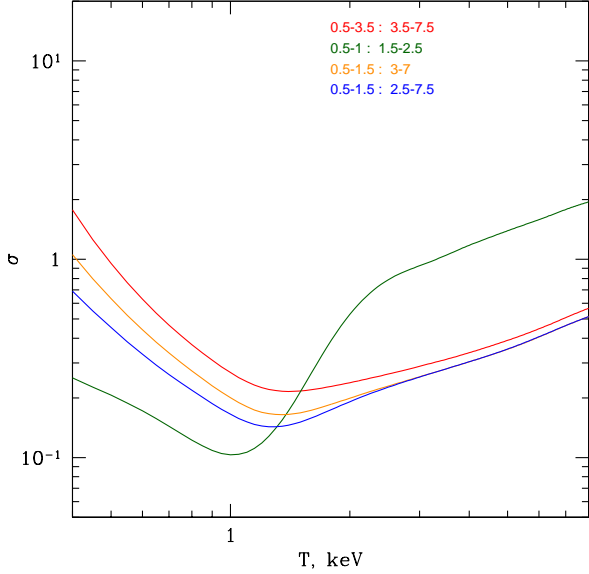


**Figure 6.** Expected RMS ( $\sigma$ ) of the manipulated image [see eq. (20)] with isothermal perturbations removed. The uncertainty is calculated as a function of temperature for several pairs of energy bands (see legend). The optimal choice is achieved when  $\sigma$  is lowest. It is clear that for  $T \lesssim 1$ , keV the best choice is the pair of images in the 0.5-1.0 and 1.5-2.5 keV bands. At  $T \gtrsim 1$  keV, several other pairs (e.g., 0.5-1.5 and 2.5-7.5 keV or 0.5-3.5 and 3.5-7.5 keV) are expected to perform better. Note that only the statistical uncertainty arising from photon counting noise has been considered here.

**Table 1.** Amplitudes of the perturbations in the manipulated images for our choice of  $\alpha_0$  (excluded process) and  $\alpha_R$  (process with unit amplitude).

$\alpha_0$	$\alpha_R$	$\alpha$		
		2/3	0	-1
Amplitude, $A_\alpha$				
2/3	-1	0	2/5	1
0	-1	-2/3	0	1
-1	2/3	1	3/5	0

of each other. On the other hand, it does not provide an unambiguous identification of the EoS of the remaining perturbations. One could extract the effective EoS directly from eq. (17), although in this case, the projection of several overlapping perturbations makes the interpretation ambiguous.

### 4.3 Selection of energy bands

The selection of reference energy bands is driven by two competing requirements: (i) to obtain the maximum number of counts in each energy band and (ii) to separate the energy bands as much as possible to maximize the difference in their response to different types of perturbations, i.e., in the quantity  $\frac{d \ln \Lambda_B}{d \ln T}$ . Assuming that only pure photon counting noise is important, it is straightforward to minimize the expected RMS of the final image  $X$ , given by eq. (20), for a particular choice of  $\alpha_0$  and  $\alpha_R$  (see, e.g., Appendix in Zhuravleva et al. 2016) by choosing appropriate energy bands. Since the amplitude of perturbations with  $\alpha = \alpha_R$  does not depend on the choice of the energy band, such choice would maximize the signal-to-noise ratio for this type of perturbation. An example of optimal energy bands, tuned for removal of isothermal perturbations, is shown in Fig. 6.

### 4.4 Cross-power spectra

Often a spherically symmetric  $\beta$ -model is clearly too simple to describe the radial surface-brightness profile of a cluster, its ellipticity or any other large-scale asymmetry. One possible way to remove these large-scale asymmetries is to apply a high-pass filter to the images. In practice, the simplest recipe is to start with a spherically symmetric  $\beta$ -model  $I_B^0$ , divide the image  $I_B$  by this model, smooth the resulting image and multiply it back by the original  $\beta$ -model:

$$I_B^1(x, y) = S \left[ \frac{I_B(x, y)}{I_B^0(x, y)} \right] I_B^0(x, y). \quad (25)$$

Here  $S$  is a smoothing operator and  $I_B^1(x, y)$  is the new global model of the cluster that includes variations of the cluster emission of the desired angular size (or larger). Note that this procedure preserves the global radial trend near the center as long as the  $I_B^0$  captures the trend. Of course one can use a more complicated initial model for  $I_B^0$ , e.g., a double  $\beta$ -model, or ellipsoidal models.

The deviations of the surface brightness from the  $I_B^1(x, y)$  now contain only the perturbations on scales smaller than the width of the smoothing filter. It is straightforward to extend this approach to a fully scale-dependent analysis. Namely, one can calculate power spectra,  $P_1(k)$  and  $P_2(k)$ , and the cross-power-spectrum  $P_{12}(k)$  of the images  $J_1$  and  $J_2$ . Here  $k$  is the wavenumber. Once  $P_1$  and  $P_2$  are corrected for the contribution of the photon counting noise ( $P_{12}$  is free from such noise, because the noise is independent in two images) one can construct two scale-dependent quantities:

$$C(k) = \frac{P_{12}(k)}{\sqrt{P_1(k)P_2(k)}}, \quad (26)$$

$$R(k) = \frac{P_{12}(k)}{P_1(k)}. \quad (27)$$

The first quantity,  $C(k)$ , is the coherence that shows how well perturbations in one band correlate with perturbations in another band.  $C \approx 1$  means that the perturbations in one band are linearly related to the perturbations in the other

band (with an arbitrary, but constant proportionality coefficient across the image). In other words, perturbations with one particular effective EoS dominate. The second quantity,  $R(k)$ , is the mean proportionally coefficient. If  $C \approx 1$ , then  $R$  gives the coefficient for the dominant EoS [see eq. (17)]. If perturbations with several different EoS's contribute significantly, then  $R$  has an intermediate value among the contributing EoS's.

We also emphasize that if we are interested only in the values of  $C(k)$  and  $R(k)$ , rather than the absolute normalization of the power spectra, analysed images can be multiplied by an arbitrary large-scale weighting function  $w(x, y)$  (the same in both energy bands) before the calculation of the power spectra. ‘‘Large-scale’’ in this context means that we are interested in the values of  $C(k)$  and  $R(k)$  on much smaller scales than those characteristic for  $w(x, y)$ . The use of such a weighting function might be useful to suppress excessive noise in the intrinsically faint or underexposed regions of the images.

Thus, by calculating  $C(k)$  and  $R(k)$  one learns which type (or types) of perturbations dominate at a given spatial scale. This approach is useful for characterizing, in an objective way, many weak structures, unlike the direct manipulation of images that helps reveal only the most prominent structures directly visible in the image. Such analysis was done for M87 (Arévalo et al. 2016) and Perseus (Zhuravleva et al. 2016).

#### 4.5 X-ray and SZ images

The same approaches, outlined above, can be applied to a combination of X-ray and Sunyaev-Zeldovich (SZ) data. An equivalent of eq. (16) for SZ is

$$J_{SZ}(x, y) = \frac{\sigma_T}{m_e c^2} \frac{n_0(r) k T_0(r) \delta_n \Delta z [1 + \alpha]}{I_{SZ}^0(x, y)}, \quad (28)$$

where  $I_{SZ}^0(x, y)$  is the model of the global map of the Comptonization parameter;  $\sigma_T$  is the Thomson scattering cross section;  $k$ ,  $m_e$  and  $c$  are the Boltzmann constant, the electron mass and the speed of light, respectively. One can use eq. (28) to get an expression for  $d_{SZ} = \delta_n \Delta z [1 + \alpha]$  and do the same for  $d_X = \delta_n \Delta z \left[ 2 + \alpha \left( \frac{d \ln \Lambda_B}{d \ln T} \right) \Big|_{T_0(r)} \right]$  using eq. (16). The relation between  $d_{SZ}$  and  $d_X$  is

$$\begin{aligned} d_X &= K d_{sz}, \text{ where} \\ K &= \frac{n_0(r) \Lambda_B [T_0(r)] I_{SZ}^0(x, y)}{\frac{\sigma_T}{m_e c^2} k T_0(r) I_B^0(x, y)}. \end{aligned} \quad (29)$$

Notice, that even for an isothermal cluster the dependence on  $r$  does not cancel out because of the different dependence on  $n_0$  of the X-ray and SZ signals. If, for a prominent feature in the image, the value of  $\alpha$  is already known from X-ray analysis, then this relation can be used to determine the location  $z$ , of the feature along the line of sight, since  $z$  enters eq. (29) via  $r = (x^2 + y^2 + z^2)^{1/2}$  both in the r.h.s. and l.h.s. of the equation. Alternatively, if one can make a guess on  $z$ , one can generate an X-ray image free from isobaric perturbations (see §4.2) and then directly compare SZ and X-ray images. This approach can be used to, e.g., differentiate between the

thermal or non-thermal nature of the gas providing pressure support for AGN-inflated bubbles, or to prove that pressure perturbations are due to sound waves. In the latter case, an additional manipulated X-ray image, free from sound waves, will be useful.

## 5 ILLUSTRATIVE EXAMPLES

To illustrate the approaches outlined above, we use Chandra observations of the Perseus and M87/Virgo clusters. The advantage of using these data sets is two-fold: (i) these are the X-ray-brightest clusters in the sky and (ii) many features have already been identified by detailed analysis (e.g., Boehringer et al. 1993; Churazov et al. 2000; Fabian et al. 2003; Forman et al. 2007; Arévalo et al. 2016; Zhuravleva et al. 2016).

The Chandra images of the Perseus cluster in the 0.5-3.5 and 3.5-7.5 keV bands, divided by their respective best-fitting  $\beta$ -models are shown in Fig. 7. In the notation of §4, these are  $\tilde{J}_B$  images [see eq. (18)]. Labels in Fig. 7 mark several prominent features, which have been tentatively identified as shocks, bubbles and isobaric structures (e.g., Fabian et al. 2003; Zhuravleva et al. 2016). Those identifications are based either on the comparison of X-ray and radio images or on a detailed spectral analysis.

These images have been combined, using eq. (20), into a new set of images (Fig. 8) to remove adiabatic, isothermal and isobaric structures. As expected, proper scaling of relative weights in a linear combination suppresses the sub-structures characterized by a target EoS. The most striking is the case when isobaric structures are removed (Fig. 8 right panel). Those structures strongly dominate the original images (Fig. 7), especially in the softer band, but are completely gone in the manipulated image. The resulting image clearly shows a very symmetric figure-8-like feature, which is believed to be due to compressed gas around growing radio lobes, produced by the central AGN. The figure-8-like shape is due to projection of two nearly circular structures on either side of the nucleus. The ‘‘older’’ bubbles are also clearly seen to the North-West and to the South of the center. While most the above features have been seen before, Fig. 8, in addition, suggests that there is an envelope of decreased thermal pressure in between the inner lobes (the figure-8-like structure) and older bubbles. It likely that this envelope is due to relativistic plasma occupying a fraction of volume around the inner lobes.

Another way to characterize the observed fluctuations is to correlate the amplitudes in  $J_1(x, y)$  and  $J_2(x, y)$  pixel by pixel directly (see Fig. 9). The three lines shown in Fig. 9 correspond to the expected correlation between fluxes in the soft and hard bands for adiabatic, isothermal and isobaric fluctuations, respectively. As is clear from this figure, all large positive perturbations correspond to isobaric perturbations (blue line). In the original images (Fig. 7), those perturbations correspond to the prominent spiral-like structure. At the same time, large negative deviations follow an isothermal EoS. These perturbations correspond to X-ray cavities (radio bubbles), visible in Fig. 7 as dark patches.

To study smaller-amplitude perturbations that are too

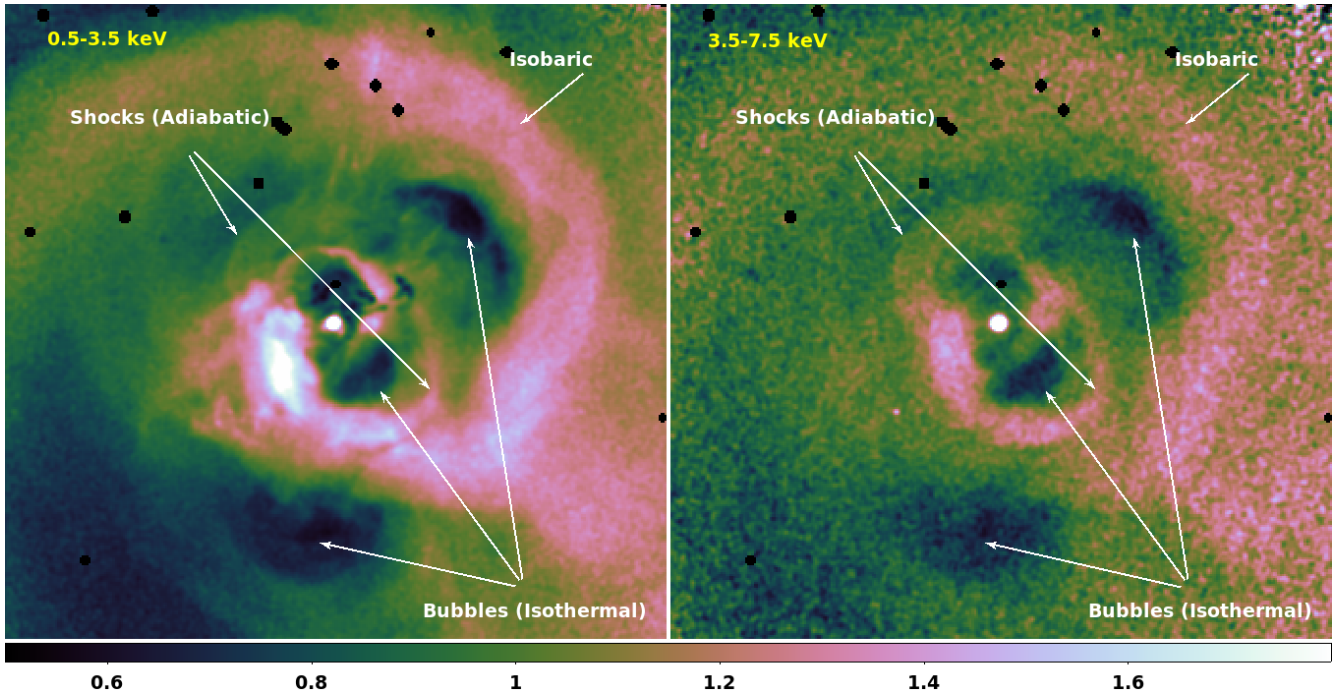


**Figure 7.** X-ray images ( $5' \times 5'$ ;  $\sim 100 \times 100$  kpc) of the Perseus cluster core divided by their respective best-fitting beta-models. Left: 0.5-3.5 keV, right: 3.5-7.5 keV. Labels mark several prominent features, which have been tentatively identified as shocks, bubbles and isobaric structures (see, e.g., Fabian et al. 2011).

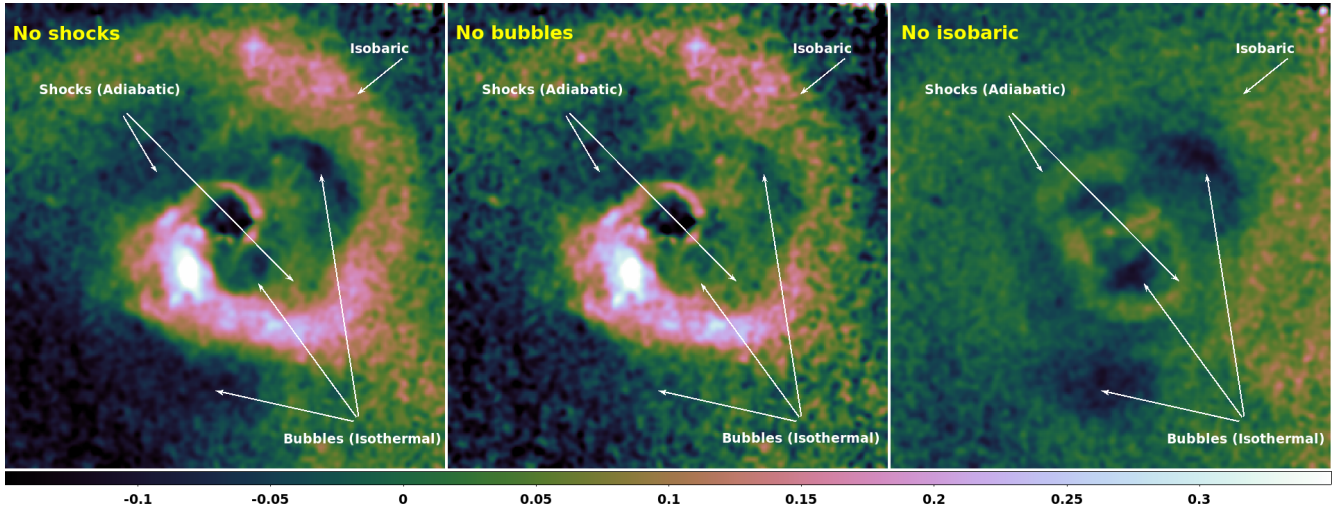


**Figure 8.** Manipulated X-ray images, based on the two images shown in Fig. 7. These two images were scaled and combined so as to exclude a particular type of perturbation. Other types of perturbations with different effective equations of state parametrized by  $\alpha = \frac{d \ln T}{d \ln n}$ , will still be present. In terms of our standard set of possible perturbations  $\alpha = \{3/2, 0, -1\}$ , the expected amplitudes  $A$  are: left panel, “no shocks”,  $A = \{0.0, 0.4, 1.0\}$ ; middle panel, “no bubbles”,  $A = \{-0.7, 0.0, 1.0\}$ ; right image, “no isobaric structures”,  $A = \{1.0, 0.6, 0.0\}$ . One can see that some of the features prominent in Fig. 7 disappear from one of the panels, suggesting that the density and temperature fluctuations obey a particular effective EoS. A feature to the West from the nucleus in the right panel is caused by cold gas absorption (see, e.g., Fabian et al. 2000).

weak to be identified individually (given the noise in the image), a cross-spectrum approach (§4.4) is a better option to characterize the mean correlation between the perturbations. Moreover, scale-dependent nature of the cross-spectrum analysis helps avoid the impact of larger-scale

asymmetries on the resulting correlations. This approach was followed for the Perseus cluster by Zhuravleva et al. (2016) and for M87 by Arévalo et al. (2016) and confirmed that isobaric perturbations dominate the overall energy budget associated with perturbations. Since all three manipu-

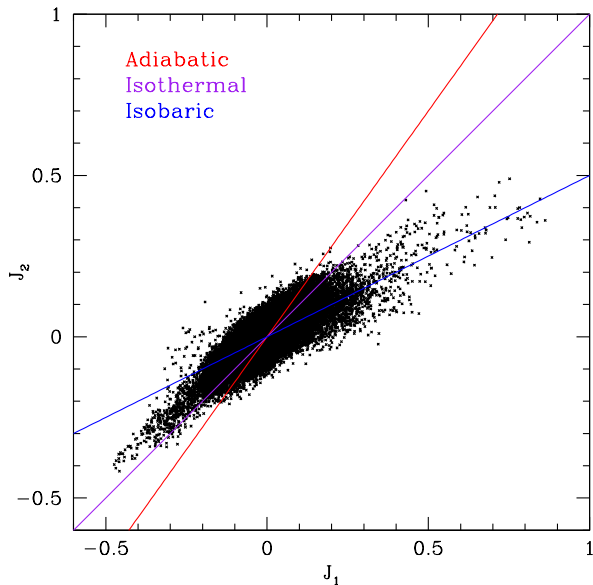


**Figure 9.** Correlation between amplitudes of perturbations in the hard and soft bands for X-ray images of the Perseus cluster. Three lines show expected dependence for adiabatic, isothermal and isobaric perturbations. Clearly, large positive deviations correspond to isobaric perturbations (cool and dense structures), while large negative deviations are almost isothermal (bubbles). For this figure a  $16' \times 16'$  image was used, i.e. larger than the images shown in Fig. 7.

lated images in Fig. 8 are shown in the same color scale, one can immediately see that in terms of variance, isobaric fluctuations clearly dominate. However, in order to estimate the energy associated with the perturbations one has either to assume a particular geometry, as was done for bubbles in many studies, or to assume that the power spectrum of the perturbations in 3D is isotropic. In the latter case, the power spectrum analysis recovers the correct normalization of the 3D power spectrum and can be used to estimate the total energy in the perturbations (see Arévalo et al. 2016; Zhuravleva et al. 2016, for details).

Fig. 10 and 11 show a similar analysis for M87 images. As discussed by Forman et al. (2007) the 3.5-7.5 keV band image of M87 (Fig.10, right) by itself provides a projected thermal pressure map (more accurately, projected square of the pressure). From Fig. 5 it is clear that for the characteristic gas temperature in M87,  $T \sim 2$  keV, the response to isobaric perturbations in this energy band is indeed close to zero. It is therefore not surprising that the manipulated image free from isobaric perturbations (Fig.11, right) look very similar to the original 3.5-7.5 keV band image.

Inspection of Figs. 8 and 11 suggests that, in terms of the density perturbation amplitude, the isobaric structures dominate, followed by bubbles (may still be isobaric, but with a significant contribution to pressure from either relativistic particles or very hot gas) and weak shocks. Such a hierarchy is best explained in a “slow” AGN feedback scenario, when much of the mechanical energy output of a central black hole is captured by the bubble enthalpy that is gradually released during buoyant rise of the bubble (e.g., Churazov et al. 2000; McNamara et al. 2000).

## 6 DISCUSSION AND CONCLUSIONS

We have presented a set of methods that help reveal the (thermodynamic) nature of the gas perturbations, observed in relaxed galaxy clusters. A modified hardness-ratio approach separates global variations of the projected temperature and small-scale substructure. As a result one can avoid excessive noise in the hardness-ratio maps, since a division of observed images, which are often noisy, is replaced by a subtraction of properly scaled images. An extension of the same technique to the “image arithmetic” works best for prominent structure and for datasets with excellent statistics, visualizing the perturbations with a given effective equation of state. For a global statistical characterization of many small perturbations, the cross-power-spectrum approach is more appropriate (see Arévalo et al. 2016; Zhuravleva et al. 2016, for details). All the methods that have been proposed are easy to implement and computationally fast.

The above analysis makes two main simplifying assumptions. Firstly, we assume that one can make a good guess about the “unperturbed” analytic model, since perturbations are calculated relative to this model. If the perturbations are on small scales, then an equivalent assumption is that the unperturbed model is very smooth on the same scales. Secondly, it is assumed that all perturbations have small amplitudes, so all terms of order  $\delta_n^2$  can be neglected. While there are always modest departures from these assumptions, the comparison of the manipulated images with the radio data and with the results of detailed spectral analysis suggests that this approach successfully classifies the types of perturbations and helps to reveal their nature.

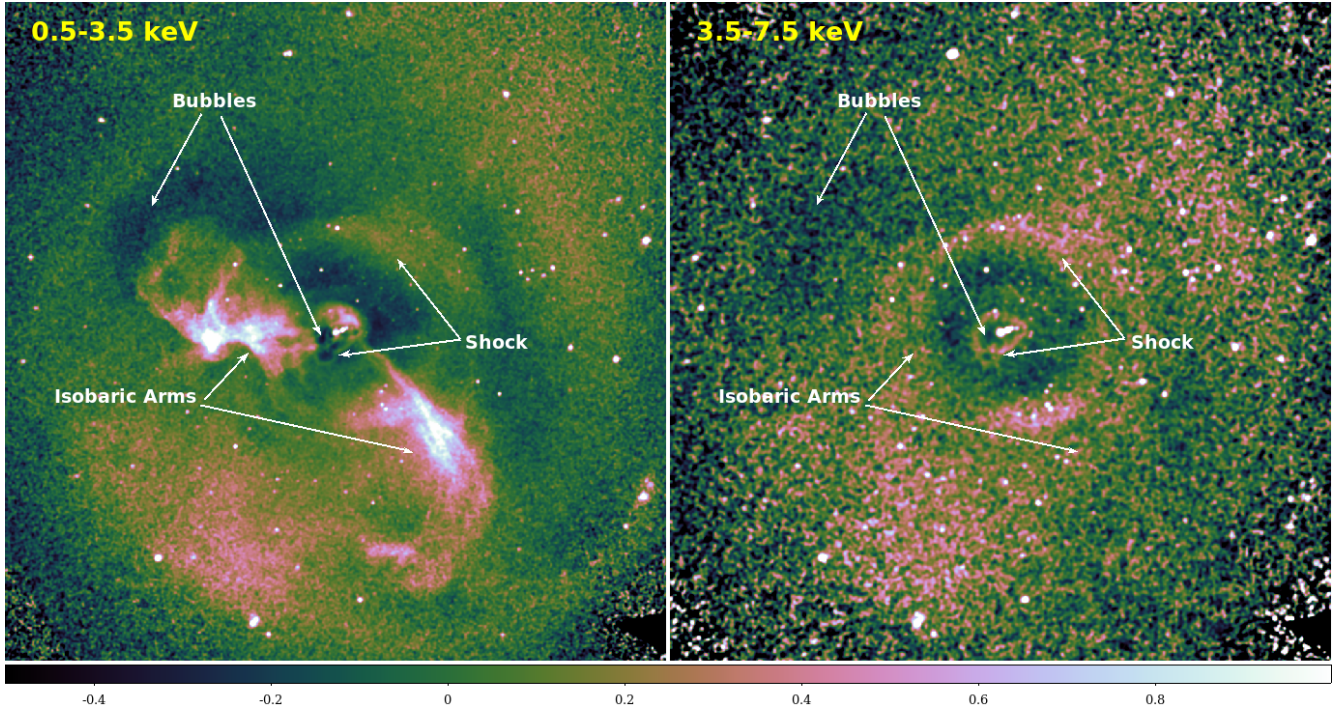


**Figure 10.** X-ray images ( $16' \times 16'$ ;  $\sim 75 \times 75$  kpc) of the M87 core divided by their respective best-fitting  $\beta$ -models (see, e.g., Forman et al. 2005, 2007). Left: 0.5-3.5 keV, right: 3.5-7.5 keV. Similar images have already been shown in Arévalo et al. (2016). Here we present them again to facilitate comparison with manipulated images of M87, shown in Fig. 11.

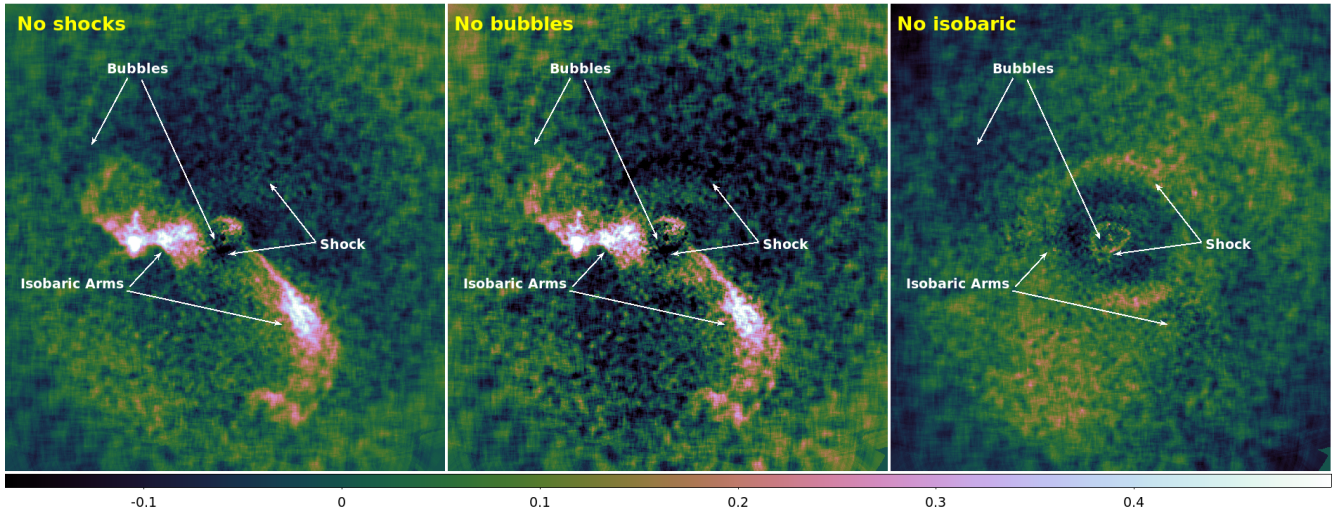


**Figure 11.** Manipulated X-ray images, based on the two images shown in Fig. 10. The procedure used to generate the manipulated images is the same as in Fig. 8. Since the characteristic temperature in M87 ( $T \sim 2$  keV) is lower than in Perseus, the 3.5-7.5 keV image by itself is expected to be free from isobaric perturbations (see Fig. 5). As the result the manipulated image in the right panel looks similar to the original 3.5-7.5 keV image in Fig. 10.

## 7 ACKNOWLEDGEMENTS

EC acknowledges support by grant No. 14-22-00271 from the Russian Scientific Foundation. WF and CJ acknowledge support from NASA contract NAS8-03060 and the Smithsonian Institution. PA acknowledges support from Fondecyt grant 1140304

## REFERENCES

- Arévalo P., Churazov E., Zhuravleva I., Forman W. R., Jones C., 2016, *ApJ*, 818, 14  
 Arévalo P., Churazov E., Zhuravleva I., Hernández-Monteagudo C., Revnivtsev M., 2012, *MNRAS*, 426, 1793  
 Arnaud K. A., 1996, *ASPC*, 101, 17  
 Boehringer H., Voges W., Fabian A. C., Edge A. C., Neu-

- mann D. M., 1993, MNRAS, 264, L25
- Cavaliere A., Fusco-Femiano R., 1978, A&A, 70, 677
- Churazov E., Forman W., Jones C., Böhringer H., 2000, A&A, 356, 788
- Churazov E., Forman W., Jones C., Böhringer H., 2003, ApJ, 590, 225
- Churazov E., Gilfanov M., Forman W., Jones C., 1996, ApJ, 471, 673
- Churazov E., et al., 2012, MNRAS, 421, 1123
- Fabian A. C., Sanders J. S., Taylor G. B., Allen S. W., Crawford C. S., Johnstone R. M., Iwasawa K., 2006, MNRAS, 366, 417
- Fabian A. C., Sanders J. S., Allen S. W., Crawford C. S., Iwasawa K., Johnstone R. M., Schmidt R. W., Taylor G. B., 2003, MNRAS, 344, L43
- Fabian A. C., et al., 2000, MNRAS, 318, L65
- Fabian A. C., et al., 2011, MNRAS, 418, 2154
- Finoguenov A., Böhringer H., Zhang Y.-Y., 2005, A&A, 442, 827
- Forman W., et al., 2005, ApJ, 635, 894
- Forman W., et al., 2007, ApJ, 665, 1057
- Gaspari M., Churazov E., 2013, A&A, 559, A78
- Gu L., et al., 2009, ApJ, 700, 1161
- Hofmann F., Sanders J. S., Nandra K., Clerc N., Gaspari M., 2016, A&A, 585, A130
- Jones C., Forman W., Vikhlinin A., Markevitch M., David L., Warmflash A., Murray S., Nulsen P. E. J., 2002, ApJ, 567, L115
- Kaastra J. S., Mewe R., Nieuwenhuijzen H., 1996, in Yamashita K., Watanabe T., eds, UV and X-ray Spectroscopy of Astrophysical and Laboratory Plasmas. Universal Academy Press, Tokyo, p. 411
- Kawahara H., Suto Y., Kitayama T., Sasaki S., Shimizu M., Rasia E., Dolag K., 2007, ApJ, 659, 257
- Kawahara H., Reese E. D., Kitayama T., Sasaki S., Suto Y., 2008, ApJ, 687, 936
- Markevitch M. L., Sarazin C. L., Irwin J. A., 1996, ApJ, 472, L17
- Markevitch M., 1996, ApJ, 465, L1
- McNamara B. R., et al., 2000, ApJ, 534, L135
- Roediger E., Kraft R. P., Forman W. R., Nulsen P. E. J., Churazov E., 2013, ApJ, 764, 60
- Roncarelli M., Etti S., Borgani S., Dolag K., Fabjan D., Moscardini L., 2013, MNRAS, 432, 3030
- Sanders J. S., Fabian A. C., 2007, MNRAS, 381, 1381
- Schuecker P., Finoguenov A., Miniati F., Böhringer H., Briel U. G., 2004, A&A, 426, 387
- Shibata R., Matsushita K., Yamasaki N. Y., Ohashi T., Ishida M., Kikuchi K., Böhringer H., Matsumoto H., 2001, ApJ, 549, 228
- Smith R. K., Brickhouse N. S., Liedahl D. A., Raymond J. C., 2001, ApJ, 556, L91
- Zhuravleva I., Churazov E., Kravtsov A., Lau E. T., Nagai D., Sunyaev R., 2013, MNRAS, 428, 3274
- Zhuravleva I., et al., 2014, Nature, 515, 85
- Zhuravleva I., et al., 2016, MNRAS, 458, 2902
- ZuHone J. A., Kunz M. W., Markevitch M., Stone J. M., Biffi V., 2015, ApJ, 798, 90